Viewing stomata in action: Autonomous *in planta* imaging of individual stomatal movement links morphology and kinetics

T. E. van den Berg, R. G. P. Sanders, E. Kaiser and J. Schmitz

Summary

Stomata regulate plant gas exchange with the environment, balancing between water loss and CO_2 uptake. Gas exchange dynamics are influenced by traits such as stomatal morphology, size and density, which are commonly investigated using imprints and manual microscopy, methods that are destructive and time consuming. Moreover, these microscopic properties are statically sampled and related to the dynamic ensemble behavior: gas exchange of an entire plant or part of a leaf. Knowledge on how morphology, size and density of stomata influence the movement of individual stomata is limited. We developed a compact microscope system that can measure the kinetics of tens of stomata *in vivo* simultaneously, with sub-minute time resolution. The system can be deployed in the plant's growth environment, at minimal impact on leaf microclimate. The characteristics of our microscope and data analyses are described, and we demonstrate its capabilities on *Chrysanthemum morifolium* with novel insight into individual stomata's contribution to water-use efficiency.

Introduction

Due to climate-change driven rises in temperature and Vapor Pressure Deficit (VPD) (Novick *et al.*, 2016) and decreased rainfall in many agricultural areas (Dore, 2005), future crop yields are coming under pressure. Adaptation of agriculture is therefore essential to maintain food security for an increasing world population (Anderson *et al.*,

31   2020). A pillar for agricultural adaptation is the development of

32   varieties with increased water-use efficiency (WUE). To achieve this,

33   we need to thoroughly understand the role that stomata play in plant

34   WUE, defined as the rate of photosynthesis divided by the rate of

35   transpiration (Bertolino *et al.*, 2019; Buckley, 2019; Lawson & Vialet-

36   Chabrand, 2019; Nadal & Flexas, 2019), to breed for stomatal traits

37   underlying high WUE.

38   Stomata are the microscopic pores on plant leaves that

39   regulate their gas exchange, by dynamically opening and closing in

40   response to environmental and intrinsic stimuli (Lawson & Matthews,

41   2020). Their dynamic behavior (Lawson & Vialet-Chabrand, 2019),

42   morphology and density (Bertolino *et al.*, 2019; Duursma *et al.*, 2019)

43   are important for plant WUE. Stomatal conductance to CO_2 diffusion

44   into the leaf facilitates photosynthetic CO_2 fixation in the mesophyll,

45   and stomatal movement broadly aims to balance the CO_2 taken up by

46   photosynthesis with the water vapor lost through transpiration. Light

47   intensity changes of ~25-50 fold on single leaves are frequent in the

48   crop growth environment (Kaiser *et al.*, 2018). When the light

49   intensity drops, the photosynthetic demand for CO_2 decreases near-

50   instantaneously, while stomatal closure proceeds much more slowly.

51   Hence, stomata that at that moment are open more than strictly

52   necessary for CO_2 demand, waste water through unnecessary

53   transpiration. Likely, fast-closing stomata are thus more water use

54   efficient.

55   Stomatal clustering and density have major effects on WUE. The

56   tendency to form clusters of stomata, compared to evenly spaced out

57   stomata, negatively affects their function (and thereby WUE), by

58   decreasing their effective response speed (Lehmann & Or, 2015).

59   Higher stomatal density negatively impacts WUE, by increasing

60   stomatal conductance under dark conditions, because stomata are

61   often not fully closed (Duursma *et al.*, 2019). However, high stomatal

62   density may increase stomatal speed and thereby WUE in fluctuating

63   light, as it tends to correlate with small stomatal size (Bertolino *et al.*,

64   2019; Lawson & Matthews, 2020), indicating the complexity of

65   stomatal trait effects on WUE.

66   An increase in light intensity quickly causes photosynthetic demand

67   for CO_2 to increase, as biochemical limitations are lifted in the first

68   minutes of photosynthetic induction (Sakoda *et al.*, 2021). To meet

69   this demand for CO_2, stomata need to open to increase the rate of

70   diffusion of CO_2, leading to a transient limitation of photosynthesis

71   while opening. Transient limitations of photosynthesis in shade-sun

72   transitions cost an estimated 10-40% of potential crop CO_2

73   assimilation (Long *et al.*, 2022). More efficient, fast-responding

74   stomata could thus result in a CO_2 assimilation increase (McAusland

75   *et al.*, 2016; Xiong *et al.*, 2018, 2022; Deans *et al.*, 2019; Acevedo-

76   Siaca *et al.*, 2020, 2021; De Souza *et al.*, 2020; Taylor *et al.*, 2020;

77   Eyland *et al.*, 2021), leading to similar potential increases in crop yield

78   (Garcia *et al.*, 2023).

79   Stomatal dynamics are most frequently studied using leaf-level gas

80   exchange measurements, and are then related to static microscopic

81   observations of e.g. leaf epidermal peels to stomatal density and

82   morphology. Measurements of bulk stomatal behavior, such as those

83   of leaf gas exchange, hide the variation in dynamics between

84   individual stomata (Kaiser & Paoletti, 2014), and studies that have

85   resolved individual stomatal dynamics are relatively rare (Kaiser &

86   Kappen, 1997, 2000, 2001; Kaiser, 2009; Grantz *et al.*, 2018).

87   Moreover, minimizing the boundary layer of still air surrounding the

88   leaf, as is common in gas exchange measurements (Busch *et al.*, 2024),

89   limits the study of stomatal behavior under frequently occurring

90   natural conditions, when a significant boundary layer is present.

91   Therefore, information is lacking on how local morphology and

92   density influence the ensemble of individual stomatal dynamics. Such

93   characteristics could lead to a better understanding of stomatal

94   control and thereby to breeding targets for WUE and yield (Haworth

95   *et al.*, 2021). Additionally, it is essential to study such characteristics

96   in the field, e.g. to understand how plants with altered stomatal

97　characteristics　respond　to　multiple　stresses　in　different

98　developmental phases (Bertolino *et al.*, 2019).

99　Here, we describe a newly developed portable microscope, which can

100　measure the opening and closure of tens of individual stomata

101　simultaneously in the growth environment. Our method innovates on

102　previous methods by selective use of green light for imaging and blue

103　and red light as actinic light. In addition, we imaged the entire field of

104　view (FOV) of the leaf's surface. We did this by creating large image

105　stacks that were used to create leaf surface projections, in contrast to

106　autofocus of single pores. This enabled us to relate stomatal dynamics

107　to microscopic characteristics of the stomatal environment on the

108　epidermis such as the distance to other stomata. Acquisition and

109　analyses were largely automated, facilitating easy measurements. We

110　demonstrated our method on leaves of *Chrysanthemum morifolium,*

111　a greenhouse crop whose stomatal behavior can limit vase life

112　(Fanourakis *et al.*, 2021) and the rate of photosynthetic induction

113　(Zhang *et al.*, 2022).

Materials and Methods

Microscope

116　The design of our microscope focused on obtaining images with sub-

117　micrometer resolution at different focus planes to resolve the 3D

118　surface of the leaf with sub-minute time resolution. Additionally, the

119　design aimed to be minimally invasive to the leaf's microclimate.

120　　　We achieved high optical resolution with high quality optics

121　(plan APO series objectives, Mitutoyo, Japan and TTL200-S8 tube lens,

122　Thorlabs, United States), verified with a calibration target (micro V2,

123　Opto, Germany). The 20x objective (NA 0.42) enabled imaging of

124　~0.45 mm^2 (722x625 μm) of the leaf's surface. High time resolution of

125　stacks of 100 images spaced 1 μm apart on the axis parallel to the

126　imaging plane (z-axis; below the 1.6 μm depth of focus of the

127　microscope objective) was achieved with a fast and accurate step

128　motor (Z812, Thorlabs, United States, range of 12 mm, 0.2 μm

129   precision), which was controlled with autofocus software and a CMOS

130   camera (BFS-U3-244S8M-C; Teledyne-FLIR, Wilsonville, OR, USA). The

131   high sensitivity of the camera and on-camera pixel binning (2x2)

132   allowed us to achieve good quality images at a relatively low light

133   intensity (50 ± 10 µmol photons $m^{-2} s^{-1}$) and integration time (400 ±

134   100 ms). The use of long working distance objectives (20 mm) and leaf

135   clips that were laser-cut from transparent polycarbonate with 2 mm

136   neoprene cushions allowed us to clamp and image the leaf with low

137   obstruction to air flow and light. Imaging was strictly done with green

138   light (Effiring 525 nm; Effilux, Hürth-Efferen, Germany) in darkfield by

139   filtering light that passed through the objective with a bandpass filter

140   (FB550-40, 550 ± 8 nm, FWHM 40 ± 8 nm; Thorlabs, Newton, NJ, USA).

141   Monochromatic light was chosen, because it boosted image quality

142   by limiting chromatic aberrations. Green light was selected because

143   of its high reflectance and transmission by the leaf, higher optical

144   resolution achievable compared to near-infrared and a maximum

145   sensitivity of the camera in the green waveband. Optimization of

146   imaging light was achieved before each automated measurement by

147   manually changing the emission angle and diffusivity (by changing the

148   opacity of the window) of the imaging light. Blue-red actinic

149   illumination was emitted by a LED lamp (444/661 nm, 20/12 nm

150   FWHM, 52/48%; Seven steps to heaven, the Netherlands). Both

151   actinic and imaging light were controlled via LabVIEW (2018, National

152   Instruments, Austin, TX, USA) and intensity calibrated at the leaf

153   position with a PAR quantum sensor (Li-190R; Li-Cor Biosciences,

154   Lincoln, NE, USA). Leaves were clamped in the microscope leaf holder

155   equipped with embedded magnets at four contact points. The

156   portable microscope was mounted on a tripod and therefore

157   adjustable in height and angle to target leaves in a plant canopy (Fig.

158   1). Leaf Temperature and PAR intensity fluctuations during the

159   measurement were recorded with a leaf clip holder (2020-B)

160   connected to a portable fluorometer (MIN-PAM; Walz, Effeltrich,

161   Germany).
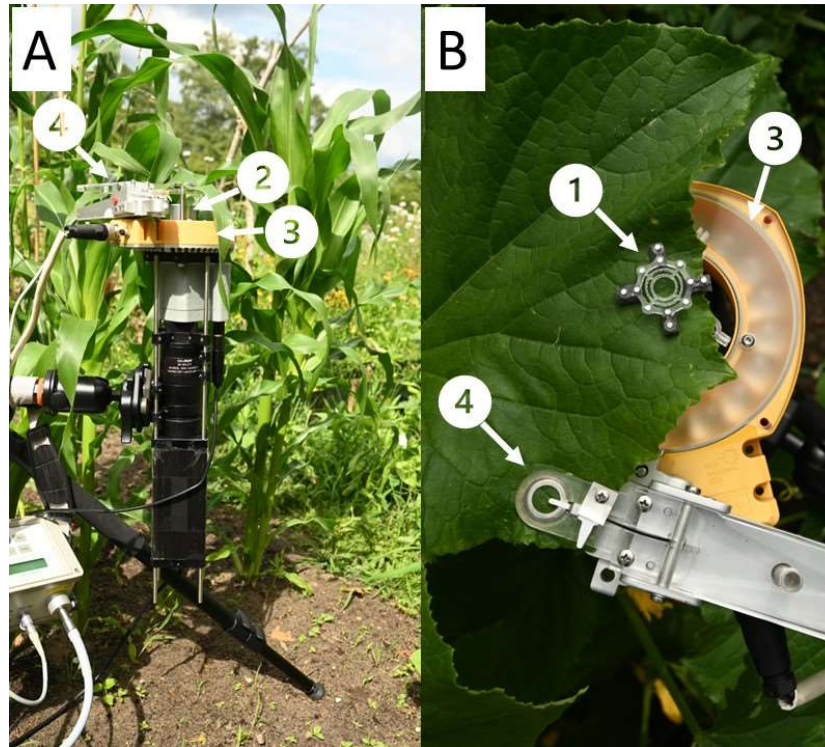
Figure 1. Example of the microscope in use at the vegetable garden of the University of Twente (the Netherlands). A. Side view of the entire microscope with a leaf of Zea mays clamped in the holder. B. Top view of a leaf of Cucumis sativa clamped in the holder. The leaf clip (1) holds the leaf in place via magnets embedded in the polycarbonate framework. Neoprene cushions ensure a minimal effect of the clamping on the surface of the leaf. The microscope objective (2) can focus automatically and the ring light (3) provides illumination for microscopy. The leaf clip from the mini-PAM (4) records fluctuations in PAR as well as ambient air temperature (A) or leaf temperature (B).

Software

Acquisition

The data acquisition software was developed in Labview. Camera settings, number of images per stack with different focus planes on the z-axis (z-stack) and stack depth, imaging and stimulus light intensity and duration, as well as autofocus settings that determined the position of the stack's center (methods: Roberts, Sobel, Gradient (Lthi *et al.*, 2010)) were controlled via Labview's user interface. Full protocol files with imaging, light timing as well as light intensity settings can be loaded into the software with a graphical user interface for inspection.

Analyses

Acquired z-stack images, in 16bit TIFF format belonging to each z-stack, were processed in several stages (Fig. 2) using Fiji open-source

187   software (Schindelin et al., 2012). Images were denoised (despeckle

188   and outlier removal), normalized for intensity (enhance contrast,

189   normalize) and aligned (SIFT linear stack alignment (Lowe, 2004)). SM

190   movie 1 is an example of a processed image stack. Next, the plugin

191   "extended depth of field" (Forster *et al.*, 2004) was used to generate

192   a focus projection of the leaf surface, reducing the stack to a single

193   image per timepoint. All timepoint focus projections were then

194   stacked again to generate a video of the entire experiment that was

195   again aligned to adjust for x-y axis movements of the leaf during the

196   experiment (SIFT linear stack alignment). This stack was then cropped,

197   to include only the area that was within view during the entire

198   experiment, shadow corrected with the pseudo flat field correction in

199   the BioVoxxel plugin (Brocher, 2015) and contrast enhanced using the

200   CLAHE algorithm (Reza, 2004) (Fig. 3 A-C). SM movie 2 is an example

201   of a processed video from an entire experiment, while SM movie 3 is

202   a zoomed version of a single stoma. Auto thresholding was done in

203   Percentile mode (Doyle, 1962), as it generated the best segmentation

204   of open pores for *Chrysanthemum morifolium* (Fig. 3D). SM movie 4

205   is the same video as SM movie 3 after thresholding. Stomata in the

206   stack were manually selected with the elliptical selection tool and

207   added in the region of interest (ROI) manager (ImageJ). Pore areas

208   were then quantified via the 'analyse particles' menu for each stoma

209   in the ROI manager, to quantify pore area and to generate masks for

210   visual inspection of pore shapes for the entire experiment (Fig 3D).

211   SM video 5 shows the masks generated from the stoma in SM videos

212   3 and 4.

213   Kinetics of stomatal aperture changes were loaded into Origin

214   (OriginLab Corporation, Nothampton, MA, USA) and, data of opening

215   and closing were fitted separately with the model (Vialet-Chabrand *et*

216   *al.*, 2013):

217   *Equation 1*

218    $A(t) = (A_{max-i} - A_{0-i})\, e^{-e^{(\frac{\lambda_i - t}{k_i} - 1)}} + A_{0-i}.$

219
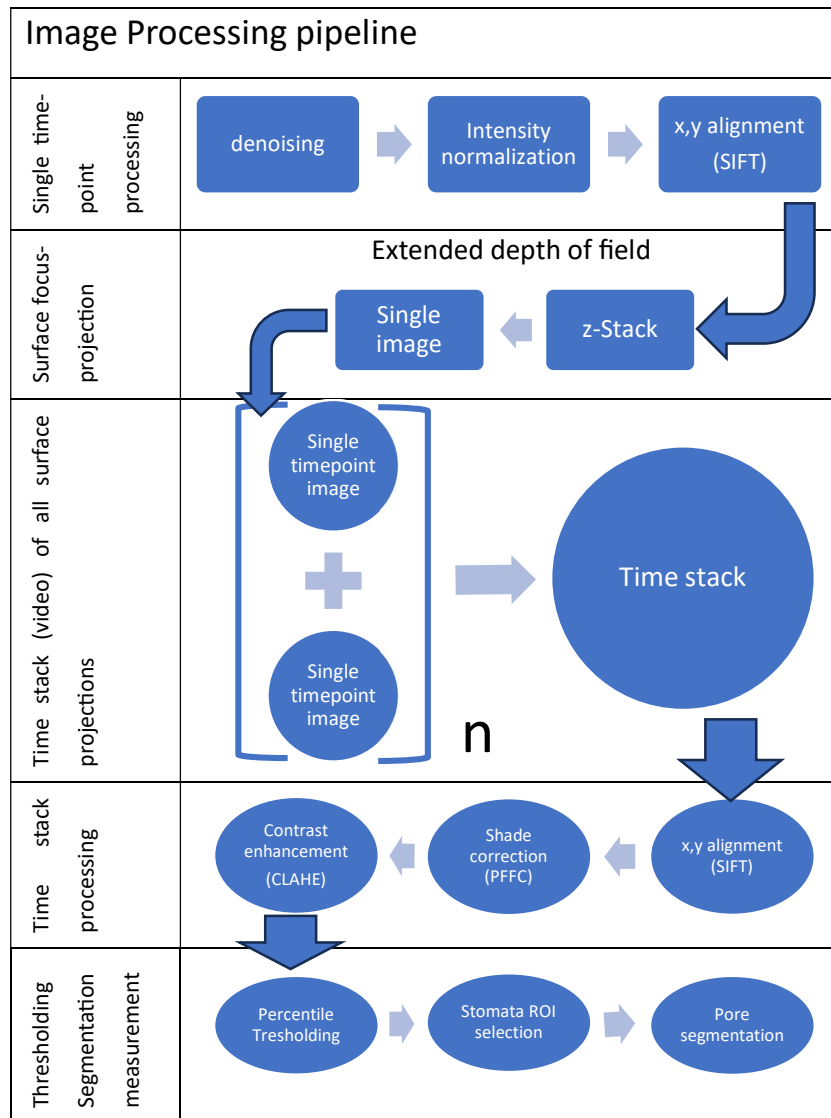
Figure 2. Flow chart of image processing pipeline. Single images belonging to an image stack were denoised and their contrast was enhanced by intensity normalization. Images with different z-axis position in a stack were then aligned to correct for minor x, y movements (surface parallel to the microscope's objective). The extended depth of field plugin processed the stack to create a single focus projection of leaf surface. Each surface projection timepoint was added together in a video of the entire experiment. The images in these videos were again aligned to correct for x, y movements, shade corrected and their contrast was enhanced. Automated thresholding of time stacks was done with Percentile mode. Stomatal positions were manually selected with the elliptical selection tool, pore area was segmented, and quantified with the analyze particles menu.

231
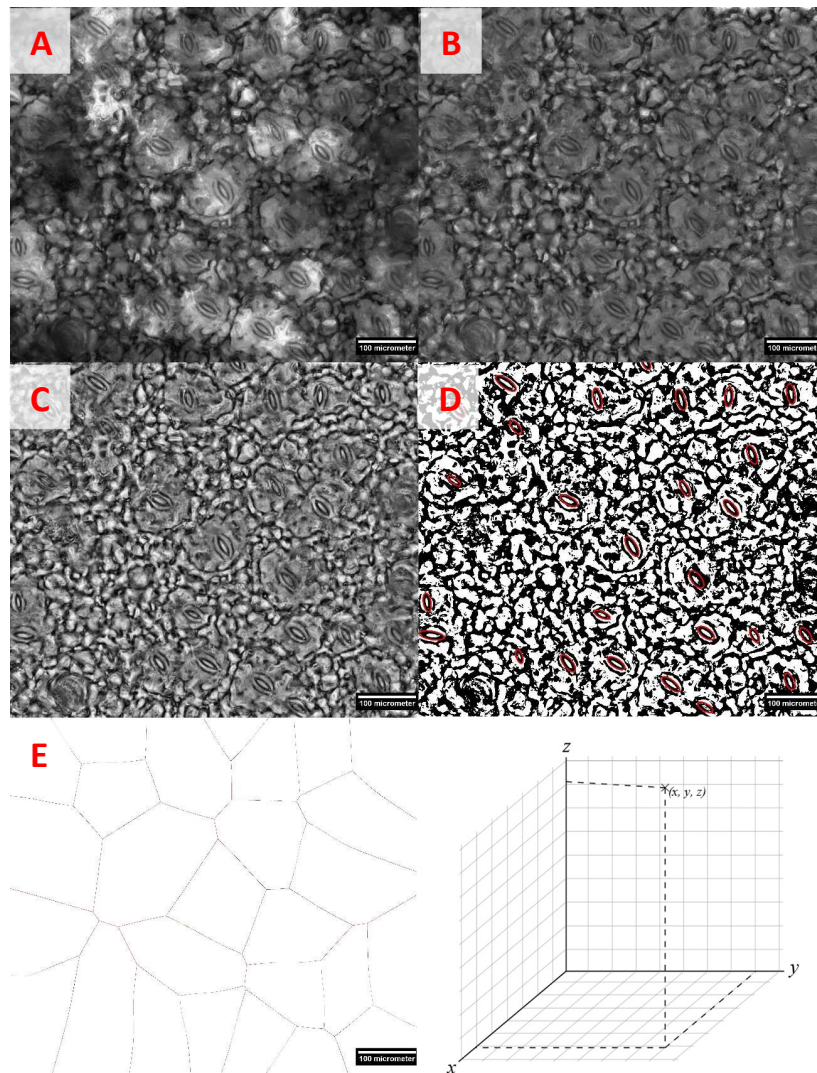
Figure 3. Example of time-stack processing with a single surface projection. A. Surface projection output from extended depth of field. B. Image in A processed with pseudo flat field correction (PFFC). C. Image in B processed with contrast limited adaptive histogram equalization (CLAHE). D. Image in C after thresholding with the Percentile method. Red ROIs are drawn manually with the elliptical selection tool. E Voronoi diagram drawn based on the elliptical selections of stomata in D. The scale bar indicates 100 micrometer.

With A(t) the stomatal aperture at time t, A_{max} the maximum aperture at steady-state, A_i the initial aperture at steady-state, λ the time lag of the response (min) and k the time constant (min), a measure of the rapidity of the response. For stomatal closure, A_{min-d} was defined as the final aperture at steady-state with A_{0-d}, the aperture at the start of the closing response. k and λ were separately quantified for open and closing responses, using subscripts i and d, respectively.

246 *Equation 2*

247 $$A(t) = (A_{min-d} - A_{0-d})\, e^{-e^{(\frac{\lambda_d-t}{k_d} - 1)}} + A_{0-d}.$$

248 Quality of fit was assessed by reduced chi squared statistic of the fit

249 (ideally close to 1), the structure in the residuals (ideally random noise

250 without structure) and error estimates of the fitted parameters

251 (ideally <10%, but no larger than 100%). SM Fig. 1 provides an

252 example of fit of the kinetics for a single stoma.

253 Some stomata were excluded from data analysis. Reasons to exclude

254 stomata were: a) Bad segmentation due to low local image quality e.g.

255 stoma shaded by trichome, b) incomplete stomatal pore on the edge

256 of an image, c) lack of pore opening after a light intensity change, d)

257 low-quality fit, as judged by χ^2, residuals and uncertainty (>100% of

258 value) in the fitted parameters.

259 Guard cell length (GCL) was measured in Fiji by manual use of the

260 straight line tool in the image at t=90 min, the timepoint where

261 stomatal aperture was generally maximal.

262 A Voronoi plot (Fig. 3E), which connects lines with equal distance to

263 the borders of each neighbouring stoma, was created via the Voronoi

264 tool (in the Fiji software), and each surface was measured via the

265 'analyse particles' menu. Resulting data were used to test for

266 relationships between the leaf area that could be assigned to a given

267 stoma ('Voronoi area') and that stoma's aperture and kinetics. Only

268 Voronoi surface areas that were fully inside the image were

269 considered in this analysis.

270

271 Because our method depends on the automated focus projection of

272 the z-stack (the reduction into a single image that represents the

273 entire surface within the FOV), we compared it to the human

274 operator: manual selection of the best focus position per pore. We

275 compared the results for ten stomata with a good distribution within

276 the FOV for 100 stacked images per 119 time points during the long

277 term shade-sun-shade transition. Further image processing,

278   segmentation and quantification of the pore area were automated

279   and following the identical protocol for both manual selection and

280   focus projection.

281   ## Plant material and growing conditions

282   ### *Chrysanthemum*

283   Experiments were conducted in a growth chamber equipped with

284   nine dimmable LED modules (DRWFR_RSE 400V 1.1D MP; Signify,

285   Eindhoven, the Netherlands) that produced a diurnal average of ~250

286   μmol m^{-2} s^{-1} of photosynthetically active radiation (PAR) at plant

287   height. A sinusoidal light pattern (16h light period, minimum PAR of

288   120 μmol m^{-2} s^{-1}, maximum PAR of 1200 μmol m^{-2} s^{-1}) was applied with

289   random drops in light intensity that mimicked natural irradiance

290   fluctuations. The timing and extent of drops in light intensity changed

291   daily, but the sinusoidal pattern and daily light sum remained fixed.

292   Temperatures were set at 23/20 °C (day/night). Relative air humidity

293   was 70%. Ventilation was 0.28-0.55 m s^{-1} of laminar flow.

294   *Chrysanthemum morifulium* (cv. Anastasia; Deliflor Chrysanten,

295   Maasdijk, the Netherlands) plants that had been grown in plastic pots

296   (diameter 14 cm, filled in with potting soil) were cut back at the third

297   or fourth node to allow for the formation of new axillary buds. Plants

298   were irrigated twice per day (at 7:00 and 19:00 h) with nutrient

299   solution, using an automatic ebb and flow system.

300   ## Stomatal aperture measurements

301   Stomatal apertures were measured on fully expanded leaves in the

302   middle between the leaf edge and the midrib. Care was taken not to

303   include veins in the FOV of the microscope, in order to maximize the

304   number of stomata in the FOV. A screen was used to shade the

305   measured plant from direct growth chamber lighting during aperture

306   measurements. Leaves were acclimated to 50 μmol m^{-2} s^{-1} blue-red

307   light and 50 μmol m^{-2} s^{-1} green imaging light for 60 minutes before

308   image acquisition was started. Image stacks were acquired every

309   minute for 120 minutes. After 30 minutes, the light intensity was

310   increased to 1000 μmol m^{-2} s^{-1} by increase of the blue-red light

311 intensity to 950 µmol m^{-2} s^{-1}. After 60 minutes, the blue-red light
312 intensity was switched back to 50 µmol m^{-2} s^{-1} (total intensity
313 including green measuring light: 100 µmol m^{-2} s^{-1}) for 30 minutes to
314 trigger stomatal closure.

Statistical Tests

316 All statistical tests were performed in Origin (OriginLab). Normality
317 tests for the distribution of fit or measured parameters were
318 performed with Shapiro-Wilkins test. KWANOVA and paired Wilcoxon
319 signed rank tests were used to test for significant differences between
320 sets of parameters that were not normally distributed. Spearman's
321 correlation was calculated between set of parameters that were not
322 normally distributed. For normally distributed data, students t-test
323 and Pearson correlations were used. The number of replicates and the
324 probability scores are mentioned with the test results.

Results

326 Our portable microscope enabled the imaging of stomatal dynamics
327 of *Chrysanthemum* in the growth environment by its selective use of
328 green light, with limited effects on stomatal movement (Jones *et al.*,
329 2022) for imaging at a low light intensity, while using stepwise
330 changes in red and blue light intensity to trigger changes in stomatal
331 aperture.

Comparison of stomatal pore area dynamics between automatic and manual selection of best focus per pore

334 The dynamics of the pore area in the focus projection images
335 (automatic) were generally well correlated with those in the manually
336 selected best single focus images (Fig. 4A, SM Fig. 2, table 1).
337 However, the pore area tended to be smaller when derived
338 automatically: pores were on average 10 µm^2 smaller in automatic
339 than in manual images, with slightly larger differences during the first
340 45 min of the experiment (Fig. 4B). To investigate if this difference in
341 pore area arose from spatial dependence of image quality, we
342 correlated the difference against positional coordinates of the
343 stomata. We found that these differences between automatic and

344   manual-derived pore area were neither correlated to the x, y position

345   of the pore in the image, nor to the distance of the pore to the image

346   edge, nor to the position in the stack of the manual images (Table 2).

347   Further, pore opening in the automatic images tended to be faster

348   than in the manual images, as indicated by the k_i parameter of the

349   model (Table 1), although this difference was not significant. Pore

350   closing speed was similar in both image sequences. In conclusion, the

351   automatic method can correctly asses the kinetic parameters of the

352   stomata but underestimates the true pore area.

353
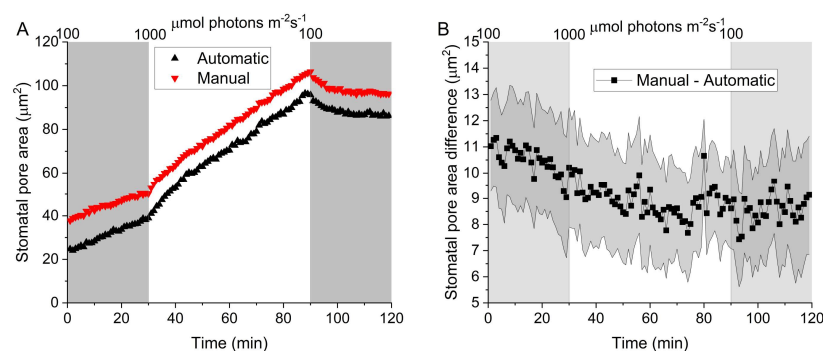
Figure 4. A Example of kinetics of one stoma analyzed with the focus projection (automatic) method or in the manually selected best single focus images (manual) demonstrating their correlation. All individual stomata curve pairs are in SM Fig 2. B Averaged difference in pore area between the same pore analyzed in the automatic images and the Manual images in all timepoints of the shade-sun-shade transition. The shaded area around the curve indicates the standard error of means. Light grey blocks indicate shade periods.

Table 1. Averaged fit parameters of the kinetic model for the pore areas in the automatic and manual images as well as Pearsons correlation coefficient between the pore area kinetics in automatic and manual images. NS indicates no significant differences between the means as tested with a paired T-test (for k_i and k_d) or non-significant correlation (P>0.05). k_i and k_d were normally distributed (Shapiro-Wilkins test). Errors indicate the SEM.

Method (n=10)	k_i (min) NS	k_d (min) NS	Pearsons r	
			automatic	manual
automatic	30 ± 2	2.8 ± 0.4	1	>0.97 (P<0.0001)
manual	36 ± 3	3 ± 1	>0.97 (P<0.0001)	1

367

Table 2 Pearsons or Spearmans correlation coefficient betweeen the average automatic-manual difference and the x, y and z coordinate of the pore and the distance to the image edge. Distance to image edge was not normally distributed in contrast to the coordinates or the z-position in the stack (Shapiro-Wilkins test)

372 *therefore Spearman correlation is used. NS indicates non-significant correlation*
373 *(P>0.05).*

Pearsons r or Spearmans ρ	X coordinate (r)	Y coordinate (r)	Distance to image edge (ρ)	z-position in stack (r)
manual-automatic	-0.16 (NS)	0.20 (NS)	0.24 (NS)	-0.36 (NS)

374

Movement of the leaf surface upon light intensity change

376 Because we recorded the changes in the position of the leaf surface
377 via automatic adjustments by the step motor of the microscope, we
378 could observe the movement of the leaf surface upon changes in light
379 intensity (Fig. 3C). Specifically, after the switch from 100 to 1000 µmol
380 m^{-2} s^{-1}, there appeared to be some shrinkage or bending of the leaf as
381 its surface moved away from the camera, whereas upon the transition
382 from 1000 to 100 µmol m^{-2} s^{-1}, the opposite happened (Fig. 5). These
383 leaf surface movements had no impact on imaging, because the FOV
384 of the leaf was always captured in focus within the stack. Leaf surface
385 movements resulted in a minor displacement of the position of the
386 leaf surface in the stack (SM Fig. 3). In conclusion, the active
387 repositioning of z-positions of each new image stack based on the z-
388 position of the leaf surface in the previous image stack, is necessary
389 because the leaf surface moves hundreds of micrometers during light
390 intensity changes.

391
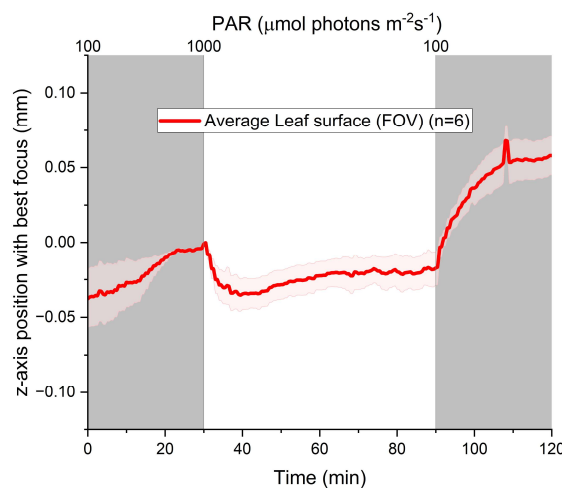
Figure 5. Position on the z-axis of the imaged area of the leaf surface where the largest area of leaf surface was in focus during the shade-sun-shade experiment. The red curve indicates the average of six biological replicates, and the shaded area indicates the standard error of the mean. The z-axis position at t=30 min was set to zero for each measurement before averaging. The Focus position (y-axis) indicates the middle position of the 100 images per one minute timepoint that were spaced 1 μm apart.

Stomatal dynamics of Chrysanthemum leaves during a shade-sun-shade transition.

To further demonstrate the power of our method, we continued to test the resolving power of the method in leaves of six plants split over two cultivation periods. After image processing, ~78% (124/158) of the stomata in the FOV were kinetically resolved (Fig. 6).

While overall stomatal aperture was in a steady-state in the initial shade condition (Figure 6, 0-30 min), individual stomata showed minor movements by either opening or closing only slightly. After the light intensity was increased, 62% of stomata (77) immediately opened their pores, while the rest showed a lag in their response of up to 40 min (Fig. 6). A duration of 60 min at 1000 μmol photons $m^{-2} s^{-1}$ was not sufficient to reach a steady-state pore opening for most stomata, which led to more uncertainty in the fitted k_i parameter than if a steady-state had been reached. Figure 7 and 8 show the distribution of the fitted parameters in violin plots.

The light intensity decrease led to an immediate closing response of thirteen stomata (13%), with the rest lagging in their response. Nineteen stomata did not close at all within the 30 min sun-shade transition (20%). These 19 stomata had a significantly higher steady-state aperture under high light intensity than the 78 stomata that closed during the shade phase (A_{max-I} 78±6>60±3, mean+SE, P<0.02, KWANOVA). In addition, they were not evenly distributed among the biological replicates: of the 19 non-closing stomata, 15 were located on one biological replicate and the remaining four stomata from two others (1 and 3 per replicate), while the remaining replicates had none. A steady-state was reached for all but five of the stomata that closed within the 30 min sun-shade transition, however this new steady-state pore aperture at lower light intensity was larger

428   than the initial steady-state level of these stomata before the opening

429   light stimulus was applied (A_{min-d} 23±3 μm^2 > A_{0-i} 13±2 μm^2, mean+SE,

430   paired sample Wilcoxon Signed Ranks Test, P<0.005).
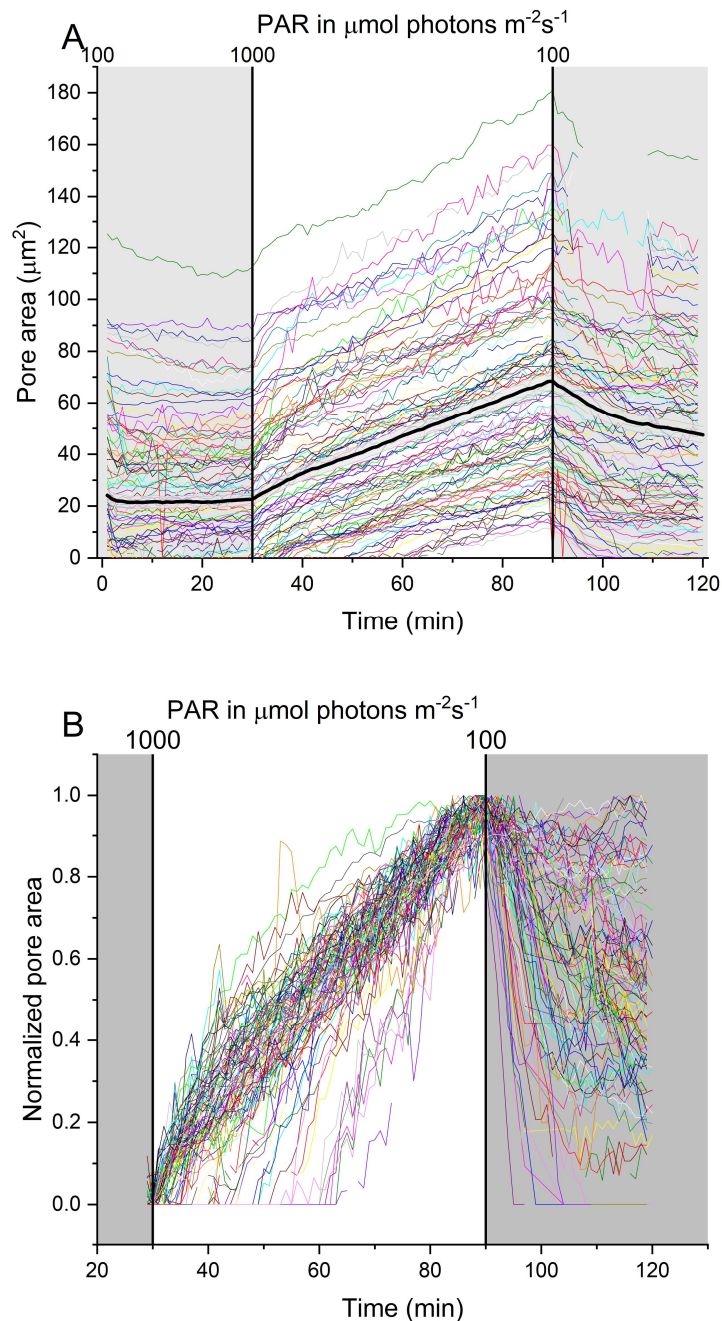
431

432   *Figure 6. A Example of stomatal pore area changes upon a shade-sun-shade*
433   *transition. Single lines show values of 124 individual stomatal pores from six*
434   *chrysanthemum plants. The thick black curve represents the average, and the grey*
435   *area the standard error of the mean. During the second shade period, a temporary*
436   *loss of focus during one measurement caused fewer data points to be recorded. B*
437   *Kinetics of all stomata shown in A, normalized to 0 at t=29 min just before the light*
438   *intensity was increased and to 1 for the maximum aperture reached at 1000 μmol*
439   *photons $m^{-2}s^{-1}$, highlighting the differences in opening lag (λ_i) and stomatal closure.*

440
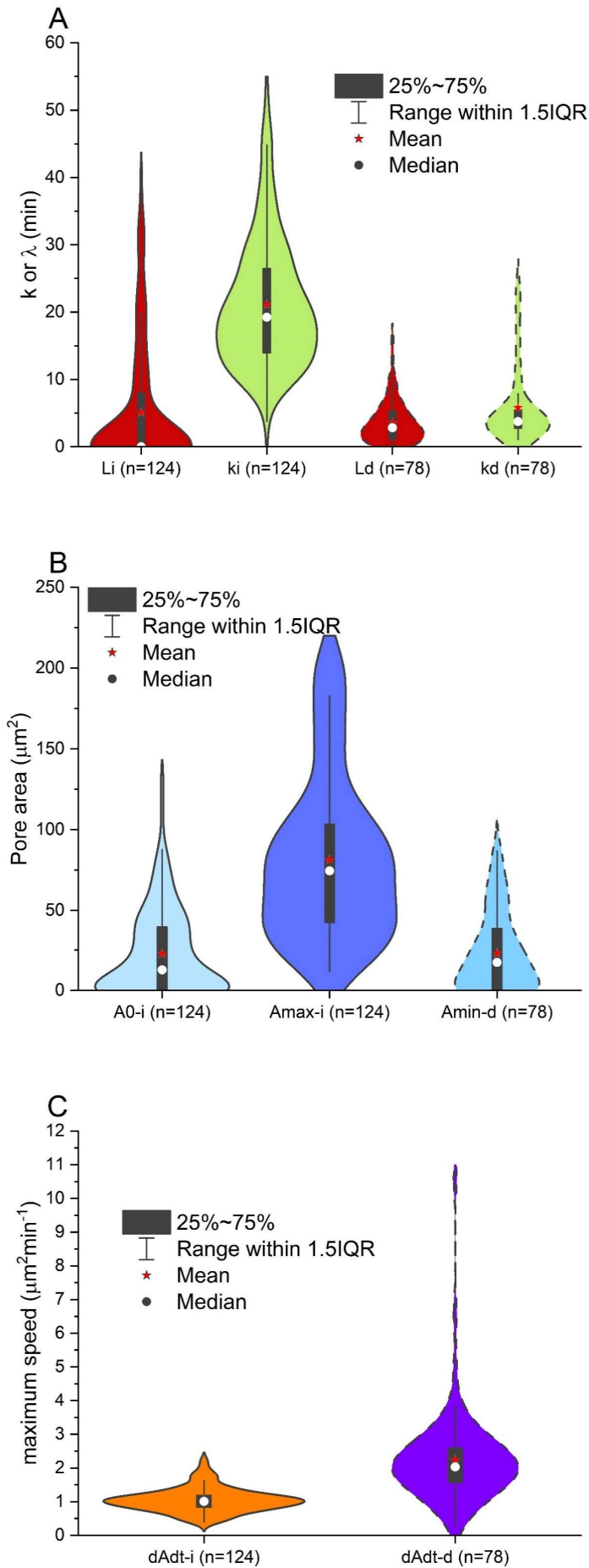
441 *Figure 7. Distributions of parameters obtained from model fits to stomatal kinetics*
442 *(raw data shown in Fig. 6). A. Opening and closing lag (Li, Ld) as well as time constants*
443 *for opening and closing (ki, kd) B. Steady-state stomatal pore area in the initial shade*
444 *period A_0, in sun period A_{max-I} and the final shade period A_{min-d}. C Maximum opening*
445 *$dAdt_i$ and maximum closing speed dAdt. Red stars represent the mean and circles the*
446 *median of the data, 25-75% indicates the position were the middle 50% of the values*
447 *in the distribution can be found and the range within 1.5 IQR indicates which part of*
448 *the distribution are not considered to be outliers.*
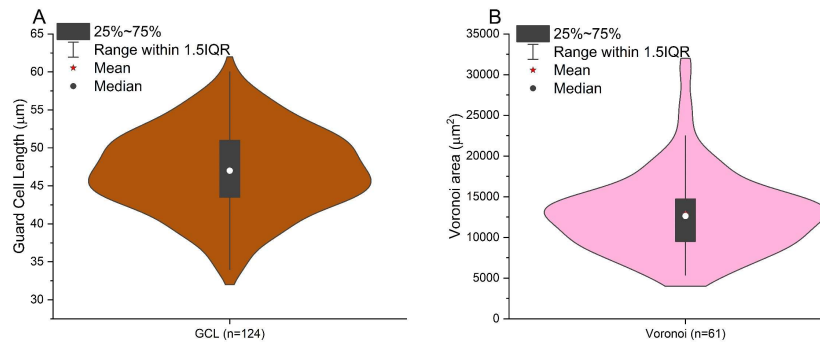
449

450 *Figure 8 Distribution of A. guard cell length (GCL) of the stomata in Fig. 6 measured*
451 *in the last image during the high light period (t=89 min) and B. Voronoi area*
452 *representing the area on the leaf that is within the shortest distance to a given stoma.*
453 *Red stars represent the mean and circles the median of the data, 25-75% indicates*
454 *the position were the middle 50% of the values in the distribution can be found and*
455 *the range within 1.5 IQR indicates which part of the distribution are not considered to*
456 *be outliers.*

457 Of the 78 stomata that opened and closed, only six

458 had a larger k_i than k_d and those k_d were the very highest among the

459 78 values (Fig. 7A), meaning that for the majority of stomata, the

460 steady-state when closing was reached faster than when opening.

461 Of all parameters, only guard cell length was normally distributed

462 (Shapiro Wilkins test, p<0.001), therefore Spearman's nonparametric

463 ρ was used to investigate correlations. A higher aperture during the

464 first shade phase (A_{0-i}) was strongly correlated with a higher maximum

465 aperture in the sun phase (Figure , A_{max-i}, ρ=0.89, p<0.001) and

466 moderately correlated to the steady-state aperture during the second

467 shade phase (A_{min-d}, ρ=0.55, p<0.001). A_{max-i} was also moderately

468 correlated to k_i (ρ=0.63, p<0.001) and $dAdt_{max-i}$ open (ρ=0.54,

469 p<0.001). The time-lag of the opening response ($λ_i$) was negatively

470 correlated to A_{0-I}, A_{max-I}, k_i, GCL, Voronoi A_{min-d}, k_d and $λ_d$, and positively

471 correlated to the closing speed $dAdt_{max-d}$. Interestingly, the time-lag of

472 the closing response ($λ_d$) was correlated to A_0 (ρ=0.54, p<0.001) and

473 A_{max-i} (ρ=0.54, p<0.001).

474
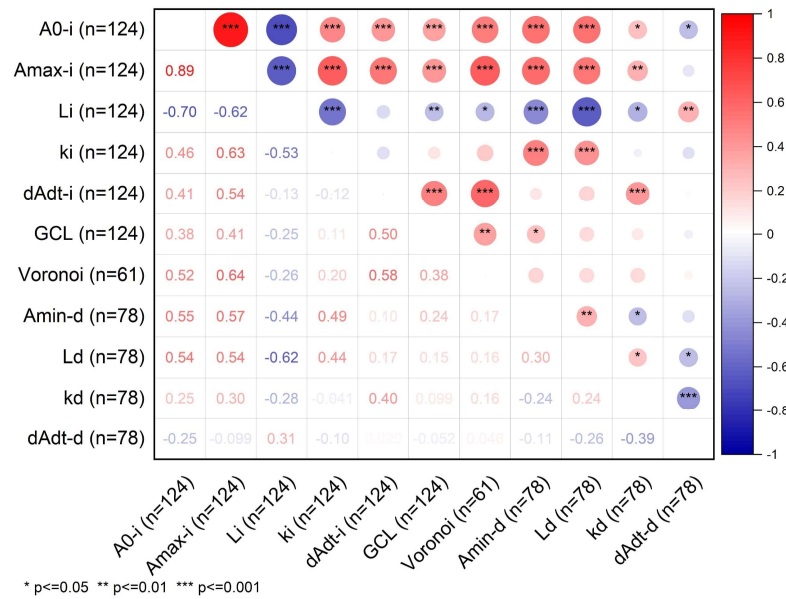
Figure 9. Spearman's correlation matrix between parameters of individual Chrysanthemum stomata (based on Fig. 7 and 8). A_0, fitted steady-state aperture under 100 µmol photons $m^{-2}s^{-1}$ PPFD. A_{max}, predicted steady-state aperture under 1000 µmol photons $m^{-2}s^{-1}$ PPFD; k_i, time constant for apertures to increase to A_{max} under 1000 µmol photons $m^{-2}s^{-1}$ PPFD; k_d, decrease from A_{max} to A_f under 100 µmol photons $m^{-2}s^{-1}$; l, initial lag in the response time of stomatal aperture to a step increase in PPFD; max dAdt, maximum rate of stomatal opening or closing to an increase or decrease in PPFD from 100 to 1000 µmol photons $m^{-2}s^{-1}$ or vice versa. Anatomical parameters of guard cell length (GCL) and width (GCW) were also compared. The Voronoi area represents the fraction of the leaf that is within the shortest distance to that stoma.

486   Among the anatomical parameters, Guard cell length (GCL) was moderately correlated to the maximum opening speed (dAdt$_{max-i}$, ρ=0.5, P<0.001), initial (A$_{0-I}$, ρ=0.38, P<0.001), maximum (A$_{max-I}$, ρ=0.41, P<0.001) and final aperture (A$_{min-d}$, ρ=0.24, P<0.05) as well as the Voronoi area (ρ=0.38, P<0.01). The Voronoi area was in addition moderately correlated with A$_{0-i}$ (ρ=0.52, p<0.001), A$_{max-i}$ (ρ=0.64, p<0.001) and the maximum opening speed (dAdt$_{max-i}$, ρ=0.58, P<0.001).

494   In conclusion, our method resolved 11 different kinetic and non-kinetic parameters for up to 78% of the stomata within the FOV to generate new insight into the WUE of individual stomata.

Discussion

498   The portable microscope presented here provides a new way to study the opening and closure of individual stomata in the growth

500 environment. This method facilitates analyses of individual stomatal

501 dynamics in relation to their local morphology and anatomy.

502 Our hardware and method are distinct from several previous

503 studies that imaged stomata *in situ* (Kaiser & Kappen, 1997, 2001;

504 Kaiser, 2009; Grantz *et al.*, 2018). The main differences and their

505 advantages and disadvantages are listed in Table 3.

506 *Table 3 Differences between this work and prior studies (Kaiser & Kappen, 1997,*
507 *2001; Kaiser, 2009; Grantz et al., 2018) with their advantages and disadvantages*

Difference	Advantage	Disadvantage	Study
525 nm versus 880 nm imaging light	Higher optical resolution	Imaging light is photosynthetically active	(Kaiser & Kappen, 1997, 2001)
Autofocus per stack instead of per pore	Imaging speed is not limited by number of stomata but only by stack size	Can cover stomata in only a small area of the leaf (~1 mm^2)	(Kaiser & Kappen, 1997, 2001; Kaiser, 2009; Grantz et al., 2018
Kinetic model fitting	Quantitative comparison of fit parameters	-	
No Gas exchange chamber	More natural boundary layer conditions	No information on leaf bulk gas exchange	(Kaiser & Kappen, 1997, 2001; Kaiser, 2009; Grantz et al., 2018

508

509 A major contrast with prior studies is that the way the leaf is clamped

510 was minimally invasive to the leaf's microenvironment, with free

511 transpiration on both sides of the leaf, because no gas exchange

512 measurements were performed. The boundary layer was not

513 regulated, reflecting a more natural condition. Another major

514 difference was the sampling of stomata: prior studies have randomly

515 sampled stomata distributed over a large area (>1 cm^2), whereas we
516 resolved as many stomatal kinetics as possible within ~1 mm^2, to
517 relate their kinetic behavior to the local morphology on the surface of
518 the leaf. In doing so, we reached a higher time resolution of, on
519 average, 21 stomata min^{-1} compared to 75 stomata once every 6-7
520 min (Grantz *et al.*, 2018). Another major difference is that we fit a
521 kinetic model to individual stomatal aperture kinetics to investigate
522 the relation of model parameters to parameters related to the local
523 morphology on the leaf surface.

524 A clear limitation of our method is the underestimation of pore area
525 compared to manual selection of the best focus per pore (Fig. 3). This
526 is especially concerning for pores that only opened minimally, as
527 these were likely found to be closed even when they were not actually
528 closed. Such pores are scored with large opening lags that are
529 erroneous. The minimal resolvable pore area is effectively limited
530 beyond the optical resolution of the microscope to ~10 μm^2 for the
531 20x objective used here. This limitation of the automated focus
532 projection method is not absolute but scales with the numerical
533 aperture of the objective. Minimally resolvable pore area can thus still
534 be improved at the cost of FOV size and working distance.   The
535 smaller pore area in the automated focus projection method is likely
536 due to differences in absolute contrast between the automatic and
537 the manual images that lead to different thresholding by the
538 percentile method. Implementation of the state-of-the art in
539 computer vision solutions, such as StomaAI (Sai *et al.*, 2023), for
540 stomatal measurements and segmentation may increase the
541 resolving power in the future.

542 The analysis of dozens of *Chrysanthemum* stomata led us to
543 the novel insight that a larger aperture at steady-state in high light
544 intensity (A_{max-i}) was positively correlated with the time lag for the
545 closing response (λ_d), with a large negative consequence for WUE
546 (Lawson & Blatt, 2014). Stomata with larger pores may suffer from a
547 larger lag in their response because of a stronger hysteresis.
548 Hysteresis is related to the opening speed at the time of the change

549   in light intensity, with opening speed ($dAdt_i$) positively correlated with

550   the maximum aperture (A_{maxi}).

551   Across a number of species, Deans *et al* (Deans *et al.*, 2019)

552   found that a large stomatal conductance at high light intensity was

553   correlated with fast closing response, to compensate in water-use

554   efficiency. We could not corroborate this for A_{max-i} and their rate of

555   closing dA/dt_{max-d} in individual stomata. *Chrysanthemum* stomata

556   with a large aperture thus have a disproportionately large negative

557   contribution on WUE normalized for their apertures, due to the

558   observed correlation between A_{max-i} and the time lag for the closing

559   response λ_i, combined with a similar closing speed as stomata with a

560   smaller aperture.

561   Stomatal size was found to be negatively correlated with WUE

562   across different *Arabidopsis* ecotypes (Dittberner *et al.*, 2018). A high

563   WUE is typically associated with a fast rate of stomatal closure

564   (Lawson & Vialet-Chabrand, 2019), and smaller stomata have indeed

565   often been observed to open or close faster than larger stomata

566   (Drake *et al.*, 2013; Kardiman & Ræbild, 2018; Durand *et al.*, 2019). In

567   contrast, we found a strong positive correlation between GCL and

568   maximum opening speed, as observed before for elliptical/kidney-

569   shaped stomata (McAusland *et al.*, 2016). The relation between

570   stomatal size and speed may thus be more complex than previously

571   assumed. This relation could be species dependent, as no correlation

572   between stomatal size and speed was found in a diverse range of

573   plants with differing stomatal morphologies and physiological

574   behaviors (Haworth *et al.*, 2018). Additionally, it may depend on the

575   type of stimulus, since e.g. step changes in light intensity and in VPD

576   often trigger different dynamics (Durand *et al.*, 2019).

577   The opening and closing speeds of stomata, that were not

578   correlated here, were found to be positively correlated in some

579   studies (Haworth *et al.*, 2021), but showed no correlation in others

580   (Xiong *et al.*, 2018). The correlation between opening and closing

581   speed may thus be species and/or condition dependent.

582   Mesophyll airspace formation is linked to functional pores

583   (Lundgren *et al.*, 2019), therefore we assumed that there was a

584   mesophyll airspace under each functional pore. We further assumed

585   that the diffusion pathway to the surrounding mesophyll was

586   approximately equal in all directions and that the majority of CO_2

587   feeding the mesophyll directly underneath the leaf surface was

588   supplied by stomata on that surface and not by stomata on the

589   opposite side of the leaf. Finally, we assumed that airspace and

590   mesophyll were homogeneously distributed below the pores. The

591   positive correlation of A_0 and A_{max} with the Voronoi area of the stoma

592   can be interpreted as the stoma matching its aperture to the local

593   demand for CO_2 from the direct mesophyll below. If a stoma has to

594   supply a larger area of mesophyll, its steady-state aperture will be

595   larger under all light conditions than that of a stoma that supplies a

596   smaller area of mesophyll. The same reasoning can be applied to the

597   opening speed: if one stoma 'feeds' a large mesophyll area with CO_2,

598   drawdown of C_i during photosynthetic induction will likely be stronger

599   compared to a stoma that supplies a smaller area, and the signal for

600   fast stomatal opening may thus be stronger. An alternative

601   explanation for the positive correlation of A_0 and A_{max} with the

602   Voronoi area may be that a larger Voronoi area supplies the guard

603   cells with more solutes, water and space to open than a smaller

604   Voronoi area.

Conclusions

605

606   We showed here that *in vivo* microscopy of stomata in the leaf's

607   growth environment could be used to generate stomatal opening and

608   closure dynamics in dozens of neighboring individual stomata. Our

609   method, which uses green light for imaging and generates focus

610   projections of the entire leaf surface within the FOV, resolved the

611   kinetics of 78% of *Chrysanthemum* stomata, on average 21 stomata

612   min^{-1} during a shade-sun-shade transition. Pore area kinetics were

613   fitted with a model developed for stomatal conductance time courses

614   and show the substantial variation between individual stomata.

615   Correlation between the fitted parameters led us to discover that

616 pores with larger apertures in high light have a larger lag time in their

617 closing response, and thereby contribute disproportionately to a

618 lower WUE.

Acknowledgements

Competing interests

625 None declared

Author contributions

627 Conceptualization T.B. and J. S., Hardware T.B. R.S. Software T.B.,

628 R.S., Growing facilities E.K., Experimentation T.B., Data Analyses T.B.,

629 Writing the first draft T.B., Critical review of the manuscript T.B., E.K.,

630 J.S., Funding J.S.

Data availability

632 All data is available upon request. For more information and

633 software updates: GitHub - Plantenna/Stomata-microscope: Non-

634 invasive microscopic imaging of individual stomatal kinetics in the

635 growth environment with high resolution

References

637 **Acevedo-Siaca LG, Coe R, Quick WP, Long SP. 2021**. Variation

638 between rice accessions in photosynthetic induction in flag leaves

639 and underlying mechanisms. *Journal of Experimental Botany* **72**:

640 1282–1294.

641 **Acevedo-Siaca LG, Coe R, Wang Y, Kromdijk J, Quick WP, Long SP**.

642 **2020**. Variation in photosynthetic induction between rice accessions

643 and its potential for improving productivity. *New Phytologist*.

644 **Anderson R, Bayer PE, Edwards D. 2020**. Climate change and the

645 need for agricultural adaptation. *Current Opinion in Plant Biology* **56**:

646 197–202.

647 **Bertolino LT, Caine RS, Gray JE. 2019**. Impact of stomatal density

648 and morphology on water-use efficiency in a changing world.

649 *Frontiers in Plant Science* **10**.

650 **Brocher J. 2015**. The BioVoxxel image processing and analysis

651 toolbox. In: European BioImage Analysis Symposium.

652 **Buckley TN**. **2019**. How do stomata respond to water status? *New*
653 *Phytologist*: 0–1.

654 **Busch FA, Ainsworth EA, Amtmann A, Cavanagh AP, Driever SM,**
655 **Ferguson JN, Kromdijk J, Lawson T, Leakey ADB, Matthews JSA,** *et*
656 *al.* **2024**. A guide to photosynthetic gas exchange measurements:
657 Fundamental principles, best practice and potential pitfalls. *Plant*
658 *Cell and Environment*.

659 **Deans RM, Brodribb TJ, Busch FA, Farquhar GD**. **2019**. Plant water-
660 use strategy mediates stomatal effects on the light induction of
661 photosynthesis. *New Phytologist* **222**: 382–395.

662 **Dittberner H, Korte A, Mettler-Altmann T, Weber APM, Monroe G,**
663 **de Meaux J**. **2018**. Natural variation in stomata size contributes to
664 the local adaptation of water-use efficiency in Arabidopsis thaliana.
665 *Molecular Ecology* **27**: 4052–4065.

666 **Dore MHI**. **2005**. Climate change and changes in global precipitation
667 patterns: What do we know? *Environment International* **31**: 1167–
668 1181.

669 **Doyle W**. **1962**. Operations useful for similarity-invariant pattern
670 recognition. *Journal of the ACM (JACM)* **9**: 259–267.

671 **Drake PL, Froend RH, Franks PJ**. **2013**. Smaller, faster stomata:
672 Scaling of stomatal size, rate of response, and stomatal
673 conductance. *Journal of Experimental Botany* **64**: 495–505.

674 **Durand M, Brendel O, Buré C, Le Thiec D**. **2019**. Altered stomatal
675 dynamics induced by changes in irradiance and vapour-pressure
676 deficit under drought: impacts on the whole-plant transpiration
677 efficiency of poplar genotypes. *New Phytologist* **222**: 1789–1802.

678 **Duursma RA, Blackman CJ, Lopéz R, Martin-StPaul NK, Cochard H,**
679 **Medlyn BE**. **2019**. On the minimum leaf conductance: its role in
680 models of plant water use, and ecological and environmental
681 controls. *New Phytologist* **221**: 693–705.

682 **Eyland D, van Wesemael J, Lawson T, Carpentier S**. **2021**. The
683 impact of slow stomatal kinetics on photosynthesis and water use
684 efficiency under fluctuating light. *Plant Physiology* **186**: 998–1012.

685 **Fanourakis D, Papadopoulou E, Valla A, Tzanakakis VA, Nektarios**
686 **PA**. **2021**. Partitioning of transpiration to cut flower organs and its
687 mediating role on vase life response to dry handling: A case study in
688 chrysanthemum. *Postharvest Biology and Technology* **181**: 111636.

689 **Forster B, Van De Ville D, Berent J, Sage D, Unser M**. **2004**. Complex
690 wavelets for extended depth-of-field: A new method for the fusion
691 of multichannel microscopy images. *Microscopy Research and*
692 *Technique* **65**: 33–42.

693 **Garcia A, Gaju O, Bowerman AF, Buck SA, Evans JR, Furbank RT,**
694 **Gilliham M, Millar AH, Pogson BJ, Reynolds MP,** *et al.* **2023**.
695 Enhancing crop yields through improvements in the efficiency of

696   photosynthesis and respiration. *New Phytologist* **237**: 60–77.

697   **Grantz DA, Zinsmeister D, Burkhardt J**. **2018**. Ambient aerosol
698   increases minimum leaf conductance and alters the aperture–flux
699   relationship as stomata respond to vapor pressure deficit (VPD).
700   *New Phytologist* **219**: 275–286.

701   **Haworth M, Marino G, Loreto F, Centritto M**. **2021**. Integrating
702   stomatal physiology and morphology: evolution of stomatal control
703   and development of future crops. *Oecologia* **197**: 867–883.

704   **Haworth M, Scutt CP, Douthe C, Marino G, Gomes MTG, Loreto F,**
705   **Flexas J, Centritto M**. **2018**. Allocation of the epidermis to stomata
706   relates to stomatal physiological control: Stomatal factors involved
707   in the evolutionary diversification of the angiosperms and
708   development of amphistomaty. *Environmental and Experimental*
709   *Botany* **151**: 55–63.

710   **Jones JJ, Huang S, Hedrich R, Geilfus CM, Roelfsema MRG**. **2022**.
711   The green light gap: a window of opportunity for optogenetic
712   control of stomatal movement. *New Phytologist* **236**: 1237–1244.

713   **Kaiser H**. **2009**. The relation between stomatal aperture and gas
714   exchange under consideration of pore geometry and diffusional
715   resistance in the mesophyll. *Plant, Cell and Environment* **32**: 1091–
716   1098.

717   **Kaiser H, Kappen L**. **1997**. In situ observations of stomatal
718   movements in different light-dark regimes: The influence of
719   endogenous rhythmicity and long-term adjustments. *Journal of*
720   *Experimental Botany* **48**: 1583–1589.

721   **Kaiser H, Kappen L**. **2000**. In situ observation of stomatal
722   movements and gas exchange of Aegopodium podagraria L. in the
723   understorey. *Journal of Experimental Botany* **51**: 1741–1749.

724   **Kaiser H, Kappen L**. **2001**. Stomatal oscillations at small apertures:
725   Indications for a fundamental insufficiency of stomatal feedback-
726   control inherent in the stomatal turgor mechanism. *Journal of*
727   *Experimental Botany* **52**: 1303–1313.

728   **Kaiser E, Morales A, Harbinson J**. **2018**. Fluctuating light takes crop
729   photosynthesis on a rollercoaster ride. *Plant Physiology* **176**: 977–
730   989.

731   **Kaiser H, Paoletti E**. **2014**. Dynamic stomatal changes. In: Tausz M,
732   Grulke N, eds. Plant Ecophysiology: Trees in a Changing
733   Environment. Springer Science+Business, 61–82.

734   **Kardiman R, Ræbild A**. **2018**. Relationship between stomatal
735   density, size and speed of opening in Sumatran rainforest species.
736   *Tree Physiology* **38**: 696–705.

737   **Lawson T, Blatt MR**. **2014**. Stomatal size, speed, and responsiveness
738   impact on photosynthesis and water use efficiency. *Plant Physiology*
739   **164**: 1556–1570.

740 **Lawson T, Matthews J**. **2020**. Guard Cell Metabolism and Stomatal
741 Function. *Annual Review of Plant Biology* **71**: 273–302.

742 **Lawson T, Vialet-Chabrand S**. **2019**. Speedy stomata,
743 photosynthesis and plant water use efficiency. *New Phytologist* **221**:
744 93–98.

745 **Lehmann P, Or D**. **2015**. Effects of stomata clustering on leaf gas
746 exchange. *New Phytologist* **207**: 1015–1025.

747 **Long SP, Taylor SH, Burgess SJ, Carmo-Silva E, Lawson T, De Souza**
748 **AP, Leonelli L, Wang Y**. **2022**. Into the Shadows and Back into
749 Sunlight: Photosynthesis in Fluctuating Light. *Annual Review of Plant*
750 *Biology* **73**: 617–648.

751 **Lowe DG**. **2004**. Distinctive image features from scale-invariant
752 keypoints. *International journal of computer vision* **60**: 91–110.

753 **Lthi BS, Thomas N, Hviid SF, Rueffer P**. **2010**. An efficient autofocus
754 algorithm for a visible microscope on a Mars lander. *Planetary and*
755 *Space Science* **58**: 1258–1264.

756 **Lundgren MR, Mathers A, Baillie AL, Dunn J, Wilson MJ, Hunt L,**
757 **Pajor R, Fradera-Soler M, Rolfe S, Osborne CP, et al.** **2019**.
758 Mesophyll porosity is modulated by the presence of functional
759 stomata. *Nature Communications* **10**: 2825.

760 **McAusland L, Vialet-Chabrand S, Davey P, Baker NR, Brendel O,**
761 **Lawson T**. **2016**. Effects of kinetics of light-induced stomatal
762 responses on photosynthesis and water-use efficiency. *The New*
763 *phytologist* **211**: 1209–1220.

764 **Nadal M, Flexas J**. **2019**. Variation in photosynthetic characteristics
765 with growth form in a water-limited scenario: Implications for
766 assimilation rates and water use efficiency in crops. *Agricultural*
767 *Water Management* **216**: 457–472.

768 **Novick KA, Ficklin DL, Stoy PC, Williams CA, Bohrer G, Oishi AC,**
769 **Papuga SA, Blanken PD, Noormets A, Sulman BN, et al.** **2016**. The
770 increasing importance of atmospheric demand for ecosystem water
771 and carbon fluxes. *Nature Climate Change* **6**: 1023–1027.

772 **Reza AM**. **2004**. Realization of the contrast limited adaptive
773 histogram equalization (CLAHE) for real-time image enhancement.
774 *Journal of VLSI signal processing systems for signal, image and video*
775 *technology* **38**: 35–44.

776 **Sai N, Bockman JP, Chen H, Watson-Haigh N, Xu B, Feng X,**
777 **Piechatzek A, Shen C, Gilliham M**. **2023**. StomaAI: an efficient and
778 user-friendly tool for measurement of stomatal pores and density
779 using deep computer vision. *New Phytologist* **238**: 904–915.

780 **Sakoda K, Yamori W, Groszmann M, Evans JR**. **2021**. Stomatal,
781 mesophyll conductance, and biochemical limitations to
782 photosynthesis during induction. *Plant Physiology* **185**: 146–160.

783 **De Souza AP, Wang Y, Orr DJ, Carmo-Silva E, Long SP**. **2020**.

Photosynthesis across African cassava germplasm is limited by Rubisco and mesophyll conductance at steady state, but by stomatal conductance in fluctuating light. *New Phytologist* **225**: 2498–2512.

Taylor SH, Orr DJ, Carmo-Silva E, Long SP. **2020**. During photosynthetic induction, biochemical and stomatal limitations differ between Brassica crops. *Plant Cell and Environment* **43**: 2623–2636.

Vialet-Chabrand S, Dreyer E, Brendel O. **2013**. Performance of a new dynamic model for predicting diurnal time courses of stomatal conductance at the leaf level. *Plant, Cell and Environment* **36**: 1529–1546.

Xiong D, Douthe C, Flexas J. **2018**. Differential coordination of stomatal conductance, mesophyll conductance, and leaf hydraulic conductance in response to changing light across species. *Plant Cell and Environment* **41**: 436–450.

Xiong Z, Xiong D, Cai D, Wang W, Cui K, Peng S, Huang J. **2022**. Effect of stomatal morphology on leaf photosynthetic induction under fluctuating light across diploid and tetraploid rice. *Environmental and Experimental Botany* **194**: 104757.

Zhang N, Berman SR, Joubert D, Vialet-Chabrand S, Marcelis LFM, Kaiser E. **2022**. Variation of Photosynthetic Induction in Major Horticultural Crops Is Mostly Driven by Differences in Stomatal Traits. *Frontiers in Plant Science* **13**: 1–19.

Supporting Information

SM Fig 1. Example of stomatal aperture dynamics of a single stoma and the model fit for opening (t=30-90) and closing (t=90-120). Raw aperture data is in black and the model fit curve in red.

SM Fig. 2 Stomatal aperture dynamics of focus projection images (automatic) and manually determined best single focus images (manual) demonstrating their correlation.

SM Fig. 3 Example of how the position of the best focus for a stoma can change in a stack during the shade-sun-shade experiment due to the movement of the leaf surface (Fig. 5).

SM Movie 1 Example of a processed z-stack (100images) of a single timepoint in the experiment. Stomata positions are indicated by red ovals.

SM movie 2 Example of the processed time stack (video) of a full experiment (119 focus projections of the z-stacks of each timepoint). Stomata positions are indicated by red ovals.

824   SM video 3 Example of the processed time stack (video) of a full
825   experiment, zoomed in on a single stoma.

826   SM video 4 The same video of 3 after thresholding.

827   SM video 5 The same video as 3 and 4 after segmentation.

828